Characterization of 3 PET tracers for Quantification of Mitochondrial and Synaptic function in Healthy Human Brain: [^{18}F]BCPP-EF, [^{11}C]SA-4503, [^{11}C]UCB-J

Ayla Mansur[1,4,7], Eugenii A. Rabiner[1,5,7] , Robert A. Comley[2,7], Yvonne Lewis[1,7],Lefkos T. Middleton[3,7], Mickael Huiban[1,7] , Jan Passchier [1,4,7], Hideo Tsukada[6,7] , Roger N. Gunn[1,4,7] and MIND MAPS Consortium[7]

[1]Invicro LLC

[2]Abbvie

[3]Neuroepidemiology and Ageing Research Unit, Imperial College London, UK

[4]Division of Brain Sciences, Imperial College London,UK

[5]King's College London, UK

[6]Hamamatsu Photonics

[7]MIND MAPS Consortium: Laurent Martarello, Biogen; Robert A. Comley, AbbVie; Laigao Chen, Pfizer, Adam Schwarz, Takeda; Karl Schmidt, Celgene; Paul Matthews, Imperial College London; Marios Politis, King's College London; Jonathan Rohrer, University College London; David Brooks, Newcastle University; James Rowe, University of Cambridge.

*Correspondence should be addressed to Ayla Mansur, PhD candidate, Imperial College London, Division of Brain Sciences, Hammersmith Hospital, London, W12 0NN, UK.
Email:ayla.mansur@invicro.co.uk

Short running title: Mitochondria and Synaptic PET Biomarkers

Financial Support: The project was funded by the MIND MAPS consortium,

Word Count: 5267

Mitochondrial complex 1 (MC1) is involved in maintaining brain bioenergetics, the sigma 1 receptor (σ1R) responds to neuronal stress and synaptic vesicle protein 2A (SV2A) reflects synaptic integrity. Expression of each of these proteins is altered in neurodegenerative diseases. Here we characterise the kinetic behaviour of three positron emission tomography (PET) radioligands [^{18}F]BCPP-EF, [^{11}C]SA-4503 and [^{11}C]UCB-J, for the measurement of MC1, σ1R and SV2A, respectively, and determine appropriate analysis workflows for their application in future studies of the *in vivo* molecular pathology of these diseases.

Methods

Twelve human subjects underwent dynamic PET scans including associated arterial blood sampling with each of the radioligands. A range of kinetic models were investigated in order to identify an optimal kinetic analysis method for each radioligand and enable the identification of a suitable acquisition duration.

Results

All three radioligands readily entered the brain and yielded heterogeneous uptake consistent with the known distribution of the protein targets. The optimal models determined for the regional estimates of volume of distribution (V_T) were multilinear analysis 1 (MA1) and the 2-tissue compartment (2TC) model for [^{18}F]BCPP-EF, MA1 for [^{11}C]SA-4503, and both MA1 and the 1-tissue compartment (1TC) model for [^{11}C]UCB-J. Acquisition times of 70, 80 and 60 minutes for [^{18}F]BCPP-EF, [^{11}C]SA-4503, [^{11}C]UCB-J, respectively, provided good estimates of regional V_T values.

Conclusion

These ligands can be assessed for their potential to stratify patients or monitor the progression of molecular neuropathology in neurodegenerative diseases.

Introduction

The complex and heterogeneous pathophysiology of neurodegenerative diseases represents a major challenge for the discovery and development of disease modifying therapeutics. A growing body of literature implicates cellular stress-related mitochondrial and endoplasmic reticulum (ER) dysfunction and related synaptic abnormalities as a common denominator across neurodegenerative diseases, making the mitochondrial/ER/synapse axis an attractive system to target in the search for biomarkers that can be used to monitor disease progression(*1–3*). Mitochondrial ATP production is critical for the bulk of neuronal processes, including neurotransmitter synthesis and synaptic plasticity. The mitochondrial complex 1 (MC1) is a critical component of ATP production, as it is where the first step of oxidative phosphorylation takes place(*4*). MC1 is responsible for cellular house-keeping mechanisms such as maintaining calcium (Ca^{+2}) homeostasis, producing reactive oxygen and nitrogen species (ROS and NOS) and regulating apoptosis(*4*). Altered MC1 function has been associated with cell toxicity, accelerated aging and the pathogenesis of multiple neurodegenerative diseases(*1*). *In vivo* quantification of MC1 in the brain has been made possible with the development of PET radioligand [^{18}F]BCPP-EF(*5*). Characterisation of [^{18}F]BCPP-EF kinetics in the non-human primate (NHP) brain has suggested its suitability for human evaluation, but no human data has been published to date(*6*,*7*).

A second regulator of cellular energy is the sigma 1 receptor (σ1R) which is a chaperone protein that stabilises the inositol phosphate 3 receptor (IP3R)/voltage dependent anion channel (VDAC) in the mitochondria-associated ER membrane (MAM) between the mitochondria and ER(*8*). This IP3R-VDAC channel is the principal pathway for Ca^{+2} influx from the ER stores to the mitochondrion, with ATP production rate depending significantly on Ca^{+2} concentration(*9*). σ1R is involved in protein sorting and folding, synaptic plasticity and neuro-protection, with human post-mortem evidence of altered expression in Alzheimer's disease (AD)(*10–12*). Early PET imaging studies have used the radioligand [^{11}C]SA-4503 to evaluate σ1R status in healthy, Parkinson's disease (PD) and AD cohorts, though an evaluation of the optimal imaging methodology for [^{11}C]SA-4503 has yet to be established(*13–15*).

The synaptic vesicle protein A (SV2A) is a membrane glycoprotein expressed ubiquitously on synaptic vesicles in presynaptic terminals and regulates Ca^{+2} mediated neurotransmitter release(*16*). SV2A has been shown to have a stable synaptic stoichiometry with good correlation to recognised synaptic density markers such as synaptophysin, and thus offers great promise as a marker of synaptic terminal density

in the human brain(*17*). Synaptic loss is central to all neurodegenerative disease pathology, with changes to presynaptic structure and function evident in presymptomatic stages of disease, raising interest in the use of SV2A markers(*18–20*). Quantification of SV2A has been made possible with the discovery of novel radioligand [^{11}C]UCB-J which has demonstrated excellent imaging characteristics(*21*). Recent findings have indicated a reduction in [^{11}C]UCB-J specific binding in healthy aging, as well as in patients with mild cognitive impairment (MCI) and AD(*22*,*23*).

The availability of PET radioligands [^{18}F]BCPP-EF, [^{11}C]SA4503 and [^{11}C]UCB-J enables the quantification of MC1, σ1R and SV2A, respectively, and allows us to test the hypothesis that a combination of these markers could provide a useful index of the function of the mitochondrial/ER/synapse axis depicted in Figure 1. The data utilised in this manuscript was collected from twelve healthy volunteers as part of the MIND MAPS* consortium (*see supplemental data for details). The methods identified here will be used for the future quantification of healthy volunteer and patient cohorts in the MIND MAPS programme. The primary aim here is to establish an appropriate set of image analysis workflows including optimal tracer kinetic quantification approaches and outcome measures for [^{18}F]BCPP-EF, [^{11}C]SA-4503 and [^{11}C]UCB-J in humans. A secondary aim is to explore whether MC1, σ1R and SV2A expression is altered in healthy aging.

Materials and Methods

Study Design

Data from 12 participants (7M/5F, 61±20 years, range 33-75) from ongoing studies evaluating MC1, SV2A and σ1R density in healthy volunteers, was included in this manuscript. Subjects were screened and scanned at Invicro London's Hammersmith Hospital site. Written informed consent was obtained from all subjects. Each subjects data acquisition included a structural MRI of the brain during screening and one PET scan with each of the following radioligands: [^{18}F]BCPP-EF, [^{11}C]SA-4503 and [^{11}C]UCB-J.

Radiotracer Synthesis

[^{18}F]BCPP-EF, [^{11}C]SA-4503 and [^{11}C]UCB-J were synthesised as previously described (*5*,*24*,*25*). The radiochemical purities were over 98% for all three tracers. Tracer injected dose information for each radioligand is summarised in Supplemental Table 1.

PET Acquisition

All PET scans were acquired on either a Siemens Hi-Rez Biograph 6 or Biograph 6 TruePoint PET/CT scanner (Siemens Healthcare, Erlangen, Germany) with subjects receiving all 3 PET scans on the same scanner. A low-dose Computed Tomography (CT) scan (30 mAs, 130 KeV, 0.55 pitch) was performed immediately before each PET scan in order to estimate attenuation. An intravenous cannula was inserted into a cubital or forearm vein for radioligand administration, and a second cannula was inserted into the radial artery to enable arterial blood collection. The radioligands were administered as a bolus (over 20 seconds) in a volume of 20 mL at the start of the PET scan. Dynamic emission data were acquired over 90 minutes following radiotracer administration and were reconstructed into 26 frames (frame durations: 8x15 s, 3 x 60 s, 5 x 120 s, 5 x 300 s, 5 x 600 s) using Discrete Inverse Fourier Transform reconstruction. Corrections were applied for attenuation, randoms and scatter.

Arterial Blood Acquisition

Whole blood activity was measured using a continuous automatic blood sampling system (Allogg AB, Marlefred, Sweden) acquired at a rate of 5 mL/min. Discrete blood samples were taken at 10, 15, 20, 25, 30, 40, 50, 60, 70, 80 and 90 minutes after scan start and total radioactivity concentration was evaluated in both blood and plasma in a Perkin Elmer 1470 10-well gamma counter. Discrete blood samples were used to determine the fraction of plasma radioactivity constituted by unchanged parent radioligand (*ppf*) using high-performance liquid chromatography (HPLC) analysis. For each ligand, the

plasma free fraction (f_p) was measured by ultrafiltration in triplicate using an arterial blood sample taken prior to tracer injection. Individual measurements of f_p are given in Supplemental Table 2.

MR Acquisition

Each subject had a T1-weighted MRI scan for coregistration with PET images. Scans were acquired on a Siemens 3T Trio clinical MRI scanner (Siemens Healthineers, Erlangen, Germany) with a 32-channel phased-array head coil using a 3D MPRAGE sequence (TE = 2.98 ms, TR = 2300 ms, cflip angle of 9°, voxel size = 1.0 mm x1.0 mm x1.0 mm).

Image Analysis and Processing

All image data were analysed using Invicro London's in-house PET data quantification tool, MIAKAT™ (version 4.3.7, http://www.miakat.org), that implements MATLAB (version R2016a; Mathworks Inc., Natick, MA, USA), FSL (version 5.0.4; FMRIB, Oxford, UK) functions for brain extraction and SPM12 (Wellcome Trust Centre for Neuroimaging, http://www.fil.ion.ucl.ac.uk/spm) for image segmentation and registration(*26*).

Each subject's MRI underwent brain extraction, grey matter (GM) segmentation and rigid body coregistration to a standard reference space(*27*). The template brain image and associated CIC atlas was then nonlinearly warped to the individual subject's MRI image where the following regions of interest (ROIs) were defined: brainstem (BST), substantia nigra (SN), thalamus (TH), ventral striatum (VST), caudate (CAU), putamen (PUT), hippocampus (HIP), insular cortex (INS), temporal lobe (TL), parietal lobe (PL), frontal cortex (FTCX) and the cerebellum (CER)(*28*). A centrum semiovale (CS) ROI was also generated from the automated anatomic labelling (AAL) template as defined previously for investigation as a reference region(*21*,*29*). PET images were registered to each subject's MRI image and corrected for motion using frame-to-frame rigid-body registration. Regional time activity curves (TACs) were generated for each ROI.

Arterial Input Function Modelling

Discrete blood samples acquired during the PET scan were fitted with a linear, constant and exponential model to determine the *ppf*. Optimal *ppf* models were identified for each tracer and applied to the total plasma activity curve to derive a metabolite corrected arterial input function.

Tracer Kinetic Modelling

All TACs were fitted with a one-tissue compartment (1TC) model, a two tissue compartment (2TC) model and graphical model multilinear analysis 1 (MA1) to estimate the volume of distribution (V_T)(*30*). MA1 was applied to TAC data acquired between 30-90 minutes (t*=30 minutes) for all tracers based on an initial assessment of an appropriate temporal window. V_T/f_p was also assessed as an outcome measure to explore its utility in studies where there are differences in f_p values.

CS has recently been explored as a reference region for [^{11}C]UCB-J(*21*). Given the low white matter (WM) uptake we observed for [^{18}F]BCPP-EF, [^{11}C]SA-4503 and [^{11}C]UCB-J, we conducted a preliminary assessment of the CS as a pseudo-reference region for each ligand, and used it to calculate the distribution volume ratio (DVR). Data are presented as mean (standard deviation).

Model Comparison and Selection

The performance of 1TC and 2TC models was assessed by Akaike Information Criteria (AIC) and parameter identifiability based on the percentage standard error (SE%) derived from the covariance matrix(*31*). Linear regression correlation coefficients (r^2) were used to compare performance between the graphical method MA1 and the compartmental models. V_Ts that were poorly estimated (SE%>10) were excluded from model comparisons.

Time Stability Analysis

The stability of each radiotracer over time was evaluated by exploring the performance of the tracer kinetic analysis methods for varying scan lengths. The estimated V_T values were expressed as percentages of the V_T estimated from the full 90 min scan (V_T^{90min}). These analyses were aggregated together over all subjects enabling assessment of time stability of the radiotracers in the population.

Assessment of Age Effects on outcome measures

A preliminary assessment of the effects of healthy aging on MC1, σ1R and SV2A density was conducted using correlation analysis with age as the predictor variable and the PET outcome measures and ROI volume as parameters of interest. ROI volume was normalised to whole brain volumes,

$$\%Vol_{roi} = 100 \times \frac{Vol_{roi}}{Vol_{brain}} \qquad \text{Equation 1}$$

where Vol_{roi} is the GM volume in a given ROI and Vol_{brain} is the whole brain volume. Percent rates of change per year in V_T, V_T/f_p, DVR and $\%Vol_{roi}$ were then calculated as,

$$\%\,\text{change/year} = 100 \times \left(\frac{\Delta\text{Parameter}}{\Delta\text{Age}}\right)/\text{Parameter}_{\text{mean}} \qquad \text{Equation 2}$$

Results

All twelve participants completed three 90 minute dynamic PET scans including arterial blood sampling and an MRI. A summary of demographic information and individual scan parameters for each radioligand are included in Supplemental Table 3.

Arterial Input Function Modelling

Ppf data for [^{18}F]BCPP-EF was best described by a sigmoid model with 20(8)% intact parent radiotracer at 90 minutes. [^{11}C]SA-4503 metabolite data were best described with an exponential function where *ppf* was estimated at 91(5)% at 90 minutes post-injection. [^{11}C]UCB-J metabolite data were described by a sigmoid model where the *ppf* was approximately 25(45)% at 90 minutes. Individual *ppf* and input function profiles are shown in the Supplemental Figure 1.

Tracer Kinetic Modelling

All three tracers entered the brain readily, and demonstrated a heterogenous distribution (Figure 2). [^{18}F]BCPP-EF uptake was fast and peak uptake values (SUV) ranged from 2.7 in the CS to 6.4 in the PUT at ~5-12 minutes post injection. [^{11}C]SA-4503 uptake was slow and reached peak values ranging from 2.3 in the CS to 4.9 in the CER at ~30-60 minutes post-injection. [^{11}C]UCB-J displayed fast kinetics producing SUV values ranging from 3.4 in the CS to 9.0 in the PUT, which declined steadily ~7-21 minutes post-injection.

All kinetic models tested reached convergence in the regional [^{18}F]BCPP-EF-derived TAC data (Figure 3A). V_T was robustly estimated in all ROIs explored using both 1TC and 2TC; with AIC analysis favouring the 2TC over 1TC in all cases tested. As 2TC and MA1 derived V_T were in excellent agreement (r^2 = 0.99) (Figure 4A), both were chosen as suitable modelling methods for [^{18}F]BCPP-EF. V_T values ranged from 11.9(2.0) ml/cm^3 in the CS to 34.0(6.6) ml/cm^3 in the PUT.

For [^{11}C]SA-4503, 2TC produced the most parsimonious fits to TACs in 155/156 of the cases tested as determined by AIC when compared to 1TC, however, V_T values were poorly estimated in 17/156 cases. MA1 produced good fits to the TAC data and V_T estimates were in close agreement with those reliably estimated using the 2TC model (r^2=0.97)(Figure 4B), and was therefore chosen as the appropriate kinetic model for [^{11}C]SA-4503. V_T estimates ranged from 25.1(7.0) ml/cm^3 in the CAU to 46.5(8.4) ml/cm^3 in the CER.

All 3 models produced excellent fits to [^{11}C]UCB-J TAC data (Figure 3C). AIC preferred 2TC over 1TC in 146/156 cases, however 3/156 V_T estimates were unstable with 2TC. MA1 produced good fits which were well-correlated with 1TC fits in all regions analysed (Figure 4C)(r^2=0.99). V_T estimates ranged from 5.7(0.7) ml/cm^3 in the CS to 20.6(2.1) ml/cm^{3}in the INS.

V_T estimates derived using all kinetic models are summarised for each radioligand in Table 1. Inter-subject variability of V_T estimates is depicted in Figure 5. The average percentage of coefficient of variance (%COV=$100 \times \frac{\text{mean}}{\text{SD}}$) of regional V_T estimates across all regions investigated was 19(4)% for [^{18}F]BCPP-EF, 20(6)% for [^{11}C]SA-4503 and 13(5)% for [^{11}C]UCB-J.

Time Stability Analysis

The average time stability profile for each radiotracer is presented in Figure 6. For [^{18}F]BCPP-EF 70 minutes of PET data provided good stability of V_T (Figure 6A), where the resulting V_T was 98.4(6.7)% of the final V_T. 80 minutes acquisition with [^{11}C]SA-4503 produced reliable V_T estimates that were 98.2(1.2)% of the V_T^{90min} (Figure 6B). [^{11}C]UCB-J estimates derived from a 60 minute scan duration were 98.0(1.8)% of V_T^{90min} (Figure 6C). Regional time stability analyses for each ligand are included in the supplemental materials for reference.

Assessment of DVR and V_T/f_p as outcome measures

DVR results were less variable between subjects compared to the corresponding V_T estimates except for [^{11}C]SA-4503, where DVR results were more susceptible to individual differences than were the V_T estimates (Supplemental Table 4). Correction of V_T by f_p had no significant effect on inter-subject variability for any of the ligands (Supplemental Table 5).

Assessment of age effects on outcome measures

The results of the linear regression analyses performed to investigate the relationship between age and yearly rate of change in ROI volume and V_T estimates are summarised in Table 2 and Figure 7. We observed a statically significant yearly reduction of 0.52% (r^2 = 0.50), 0.36%(r^2 = 0.59) and 0.53%(r^2 = 0.56) in TL, PL and FTCX volume, respectively (Figure 7A).

[^{18}F]BCPP-EF V_T decreased with age most GM regions with the highest reduction of 1.68%/year (r^2 = 0.42) in the CAU (Figure 7B). A similar negative trend was observed for [^{11}C]SA-4503, however none of the correlations reached significance (Figure 7C). [^{11}C]UCB-J V_T were negatively correlated with age

in all regions, with significant reductions in the THA, VSTR, CAU, INS, PL and FTCX (Figure 7D, Table 2). The magnitude of the mean rates of decrease in V_T ranged from 0.48%/year(r^2 = 0.36), in the INS to 1.83%/year(r^2 = 0.68) in the CAU.

Results of our regression analysis between DVR and age were similar to those observed with V_T (Supplemental Table 6-Figure 5A). [^{18}F]BCPP-EF V_T/f_p was negatively correlated with age in the TH, CAU, and PL, while correcting [^{11}C]UCB-J V_T by f_p masked out any prior age effects on SV2A density (Supplemental Table 7-Figure 5B).

Discussion

The current study evaluated a variety of kinetic quantification approaches for the radioligands [^{18}F]BCPP-EF, [^{11}C]SA-4503 and [^{11}C]UCB-J in the human brain. In addition, we conducted a pilot examination of the effects of age on the density of MC1, σ1R and SV2A. [^{18}F]BCPP-EF displayed reversible kinetics with the highest uptake observed in striatal regions, consistent with NHP data(*7*). [^{18}F]BCPP-EF metabolism was rapid and the TAC data were well described using both MA1 and 2TC. Our results showed a reduction of [^{18}F]BCPP-EF with age in line with preclinical experiments(*5*). Importantly, reductions in the CAU did not appear to be driven by changes in volume (Figure 7A-B, Supplemental Figure 2A-B), suggesting that striatal mitochondrial density could be particularly susceptible to aging.

The tracer characteristics of [^{11}C]SA-4503 were in agreement with initial imaging results in humans(*13*). We selected MA1 as the optimal model to describe [^{11}C]SA-4503 kinetics, as ~11% of our 2TC derived V_T estimates were poorly estimated. This was mainly due to the poor estimation of k_4 in the CAU, SN and CS, suggesting that [^{11}C]SA-4503 kinetics approach irreversibility in these regions and thus should be interpreted with caution. [^{11}C]SA-4503 signal was highest in the CER, consistent with previous mouse and initial human studies(*13*,*24*). Despite preclinical reports of an age-related increase in [^{11}C]SA-4503 signal, we did not observe any such effect in our dataset.

[^{11}C]UCB-J uptake was widespread and displayed fast kinetics that were well described by all three models in agreement with previous reports(*21*). Given the near perfect correlation between MA1 and 1TC derived V_T estimates, we suggest using either 1TC or MA1 for [^{11}C]UCB-J quantification. Consistent with recent reports of age effects on [^{11}C]UCB-J binding, we observed an effect of age on SV2A density in the CAU, where the reduction in signal remained significant following correction by f_p (*22*). It should be noted that with the exception of the CAU, the yearly rates of change in V_T were comparable to the rates of change in ROI volume, indicating that these reductions could primarily be due to volume loss**.** The future application of partial volume correction in an expanded cohort of subjects will be required in order to draw solid conclusions regarding the effect of age.

Comparison of V_T estimates for a particular radioligand requires the measured f_p to remain unchanged between subjects and experimental conditions. In our dataset, we observed a pronounced negative effect of age on f_p for [^{11}C]UCB-J (r^2 = 0.25 , p=0.10), which was not the case for [^{18}F]BCPP-EF (r^2 =

0.05, p=0.47) and [^{11}C]SA-4503 (r^2=0.08, p=0.37) (Supplemental Figure 7). We therefore corrected for [^{11}C]UCB-J V_T by subject f_p and took V_T/f_p as the primary outcome measure. Future [^{11}C]UCB-J studies should evaluate f_p and correct for any potential inter-subject or group differences, especially when studying patient groups.

Ideally, the distribution volume of nondisplaceable ligand relative to the total concentration of ligand in plasma (V_{ND}) can be directly estimated from a reference region, which is not feasible for compounds lacking a region devoid of specific binding. DVR provides a partial solution to this problem by relying on a region with low specific binding, and in theory could be used to eliminate some of the variability associated with the estimation of individual input functions. Although no known reference regions exist for [^{18}F]BCPP-EF, [^{11}C]SA-4503 and [^{11}C]UCB-J, we found that [^{18}F]BCPP-EF V_T estimates in the CS were ~50% lower than GM regions in our dataset. Similarly, [^{11}C]UCB-J V_T estimates in the CS were ~60% lower than GM regions, supporting previous suggestions of the CS as a reference region for SV2A quantification(*35*). Future blocking studies with specific MC1 and SV2A compounds should be conducted in healthy and disease cohorts to confirm the viability of CS as a reference region and obviate the need for arterial blood sampling. In the case of [^{11}C]SA-4503, V_T estimates in WM were not significantly lower than GM regions, making DVR an unsuitable outcome measure for this tracer.

Based on the results of our time stability analyses, we conclude that dynamic scanning for at least 70, 80 and 60 minutes are sufficient to reliably estimate V_T from a [^{18}F]BCPP-EF, [^{11}C]SA-4503 and [^{11}C]UCB-J scan, respectively. Our [^{11}C]UCB-J time stability results support those from a recent test-retest analysis of [^{11}C]UCB-J kinetics(*34*).

Conclusion

We have established a set of optimal tracer kinetic quantification models and outcome measures for [^{18}F]BCPP-EF, [^{11}C]SA-4503 and [^{11}C]UCB-J in the healthy human brain. We suggest that MA1 or 2TC can be used to quantify [^{18}F]BCPP-EF, MA1 should be used to quantify [^{11}C]SA-4503, while both MA1 and 1TC are suitable for [^{11}C]UCB-J quantification. Lastly, our analysis of the effect of age on this data set suggests that [^{18}F]BCPP-EF and [^{11}C]UCB-J signal in the CAU could serve as a marker of age-related mitochondrial dysfunction and synaptic loss.

Financial Disclosure

AM, ER YL, MH, JP RG are employees of Invicro LLC; RC is an employee of AbbVie; RG is a consultant for AbbVie, Biogen & Cerveau. HT is an employee of Hamamatsu Photonics.

Acknowledgements

The authors thank Elbert Perez, Ryan Janisch and Mark Tanner for their expert assistance. The authors also thank the Yale University PET Center for provision of CS regional definition.

References

1. Grimm A, Eckert A. Brain aging and neurodegeneration: from a mitochondrial point of view. *J Neurochem*. 2017.

2. Xiang C, Wang Y, Zhang H, Han F. The role of endoplasmic reticulum stress in neurodegenerative disease. *Apoptosis*. 2017.

3. Briggs CA, Chakroborty S, Stutzmann GE. Emerging pathways driving early synaptic pathology in Alzheimer's disease. *Biochem Biophys Res Commun*. 2017.

4. Sazanov LA. A giant molecular proton pump: structure and mechanism of respiratory complex I. *Nat Rev Mol Cell Biol*. 2015;16:375-388.

5. Harada N, Nishiyama S, Kanazawa M, Tsukada H. Development of novel PET probes, [18F]BCPP-EF, [18F]BCPP-BF, and [11C]BCPP-EM for mitochondrial complex 1 imaging in the living brain. *J Label Compd Radiopharm*. 2013;56:553-561.

6. Tsukada H. The use of 18F-BCPP-EF as a PET probe for complex i activity in the brain. *Methods Enzymol*. 2014;547:417-431.

7. Tsukada H, Ohba H, Kanazawa M, Kakiuchi T, Harada N. Evaluation of 18F-BCPP-EF for mitochondrial complex 1 imaging in the brain of conscious monkeys using PET. *Eur J Nucl Med Mol Imaging*. 2014;41:755-763.

8. Hayashi T, Su TP. Sigma-1 receptor chaperones at the ER-mitochondrion interface regulate Ca(2+) signaling and cell survival. *Cell*. 2007;131:596-610.

9. Su TP, Hayashi T, Maurice T, Buch S, Ruoho AE. The sigma-1 receptor chaperone as an inter-organelle signaling modulator. *Trends Pharmacol Sci*. 2010.

10. Nguyen L, Lucke-Wold BP, Mookerjee S, Kaushal N, Matsumoto RR. Sigma-1 receptors and neurodegenerative diseases: Towards a hypothesis of sigma-1 receptors as amplifiers of neurodegeneration and neuroprotection. *Adv Exp Med Biol*. 2017.

11. Francardo V, Bez F, Wieloch T, Nissbrandt H, Ruscher K, Cenci MA. Pharmacological stimulation of sigma-1 receptors has neurorestorative effects in experimental parkinsonism. *Brain*. 2014;137:1998-2014.

12. Jansen KLR, Faull RLM, Storey P, Leslie RA. Loss of sigma binding sites in the CA1 area of the anterior hippocampus in Alzheimer's disease correlates with CA1 pyramidal cell loss. *Brain Res*. 1993.

13. Sakata M, Kimura Y, Naganawa M, et al. Mapping of human cerebral sigma1 receptors using positron emission tomography and [11C]SA4503. *Neuroimage*. 2007;35:1-8.

14. Mishina M, Ishiwata K, Ishii K, et al. Function of sigma1 receptors in Parkinson's disease. *Acta Neurol Scand*. 2005.

15. Mishina M, Ohyama M, Ishii K, et al. Low density of sigma1 receptors in early Alzheimer's disease. *Ann Nucl Med*. 2008;22:151-156.

16. Wan QF, Zhou ZY, Thakur P, et al. SV2 Acts via Presynaptic Calcium to Regulate Neurotransmitter Release. *Neuron*. 2010;66:884-895.

17. Nowack A, Yao J, Custer KL, Bajjalieh SM. SV2 regulates neurotransmitter release via multiple mechanisms. *AJP Cell Physiol*. 2010.

18. Selkoe DJ. Alzheimer's disease is a synaptic failure. *Science (80-)*. 2002.

19. Reddy PH, Tripathi R, Troung Q, et al. Abnormal mitochondrial dynamics and synaptic degeneration as early events in Alzheimer's disease: Implications to mitochondria-targeted antioxidant therapeutics. *Biochim Biophys Acta - Mol Basis Dis*. 2012.

20. Milnerwood AJ, Raymond LA. Early synaptic pathophysiology in neurodegeneration: Insights from Huntington's disease. *Trends Neurosci*. 2010.

21. Finnema SJ, Nabulsi NB, Eid T, et al. Imaging synaptic density in the living human brain. *Sci Transl Med*. 2016;8.

22. Carson R, Naganawa M, Matuskey D, et al. Age and sex effects on synaptic density in healthy humans as assessed with SV2A PET. *J Nucl Med*. 2018.

23. Chen M-K, Mecca AP, Naganawa M, et al. Assessing Synaptic Density in Alzheimer Disease With Synaptic Vesicle Glycoprotein 2A Positron Emission Tomographic Imaging. *JAMA Neurol*. 2018.

24. Kawamural K, Ishiwata K, Tajima H, et al. In vivo evaluation of [11C]SA4503 as a PET ligand for mapping CNS sigma1receptors. *Nucl Med Biol*. 2000.

25. S.J. F, N. N, J. M, et al. Evaluation of [11C]UCB-J as a novel pet radioligand for imaging synaptic vesicle glycoprotein 2a (SV2A) in the human brain. *J Cereb Blood Flow Metab*. 2016.

26. Jenkinson M, Pechaud M, Smith S. BET2: MR-based estimation of brain, skull and scalp surfaces. *Elev Annu Meet Organ Hum brain Mapp*. 2005.

27. Grabner G, Janke AL, Budge MM, Smith D, Pruessner J, Collins DL. Symmetric atlasing and model based segmentation: an application to the hippocampus in older adults. *Med Image Comput Comput Assist Interv*. 2006.

28. Tziortzi AC, Searle GE, Tzimopoulou S, et al. Imaging dopamine receptors in humans with [11C]-(+)-PHNO: Dissection of D3 signal and anatomy. *Neuroimage*. 2011.

29. Tzourio-Mazoyer N, Landeau B, Papathanassiou D, et al. Automated anatomical labeling of activations in SPM using a macroscopic anatomical parcellation of the MNI MRI single-subject brain. *Neuroimage*. 2002.

30. Ichise M, Toyama H, Innis RB, Carson RE. Strategies to improve neuroreceptor parameter estimation by linear regression analysis. *J Cereb Blood Flow Metab*. 2002.

31. Akaike H. Information Theory and an Extensioon of the Maximum Likelihood Principle. *Int Symp Inf theory*. 1973:267-281.

32. Ishiwata K, Kobayashi T, Kawamura K, Matsuno K. Age-related changes of the binding of [3h]SA4503 to sigma1 receptors in the rat brain. *Ann Nucl Med*. 2003;17:73-7.

33. Kawamura K, Kimura Y, Tsukada H, et al. An increase of sigma receptors in the aged monkey brain. *Neurobiol Aging*. 2003;24:745-752.

34. Finnema SJ, Nabulsi NB, Mercier J, et al. Kinetic evaluation and test–retest reproducibility of [^{11}C]UCB-J, a novel radioligand for positron emission tomography imaging of synaptic vesicle glycoprotein 2A in humans. *J Cereb Blood Flow Metab*. 2017:0271678X1772494.

35. Koole M, van Aalst J, Devrome M, et al. Quantifying SV2A density and drug occupancy in the human brain using [11C]UCB-J PET imaging and subcortical white matter as reference tissue.

European Journal of Nuclear Medicine and Molecular Imaging. 2018.

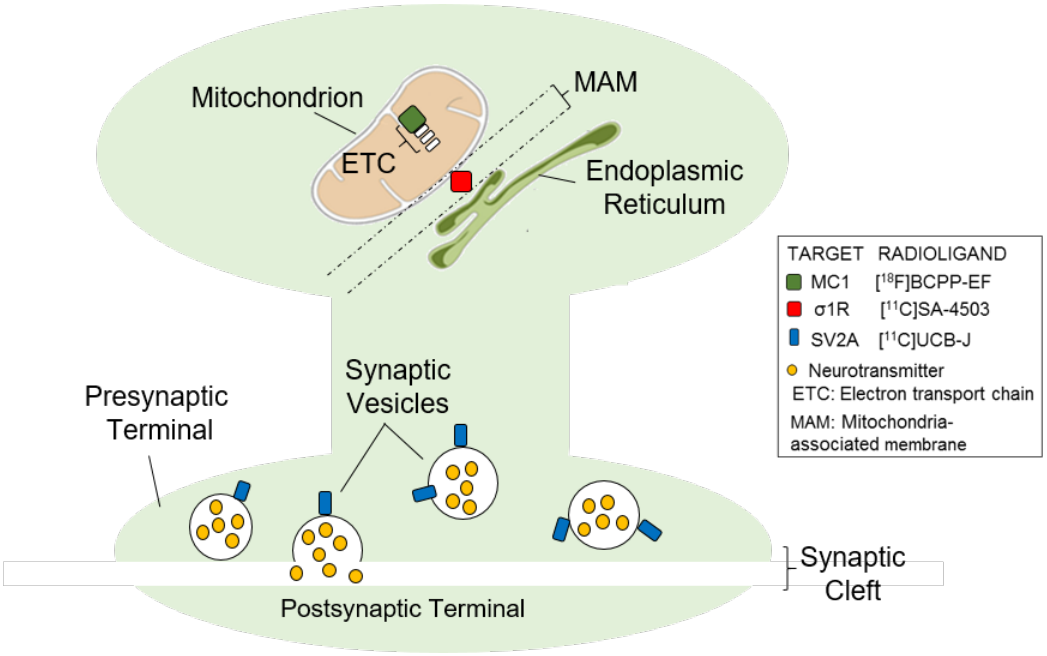

FIGURE. 1 The Mitochondrial-ER-Synaptic Axis

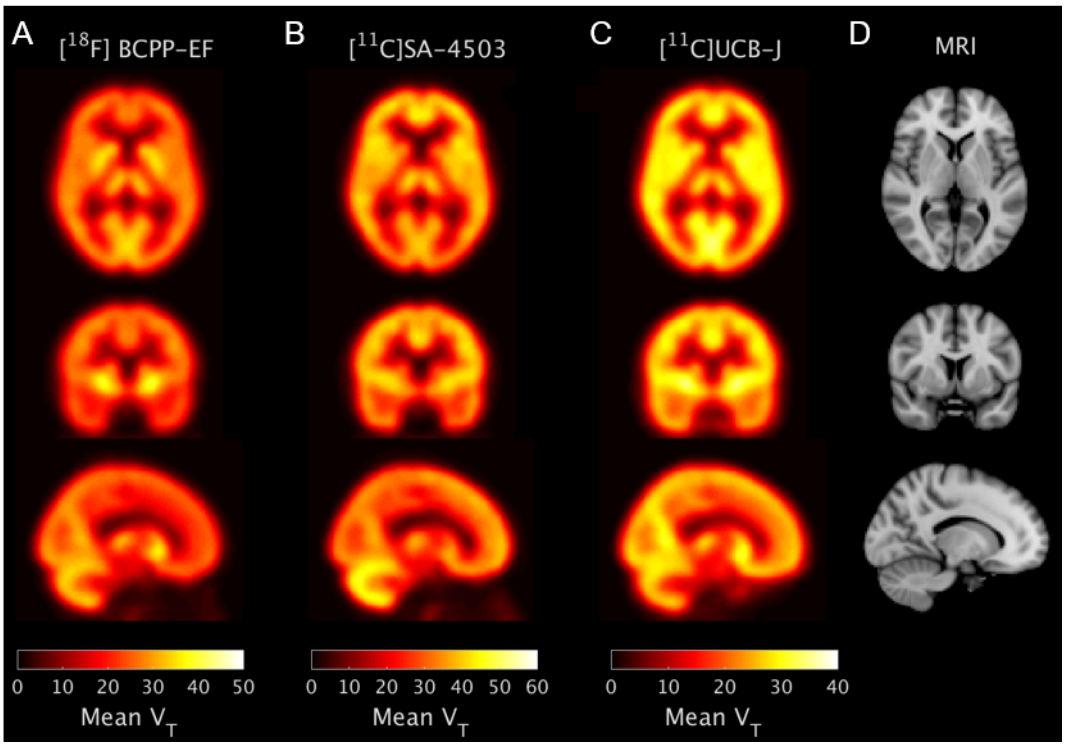

FIGURE. 2 Orthogonal cross-sections of average parametric V_T images (n = 12) generated by Logan Graphical analysis of (A)[^{18}F]BCPP-EF, (B)[^{11}C]SA-4503, and using 1TC for (C)[^{11}C]UCB-J.

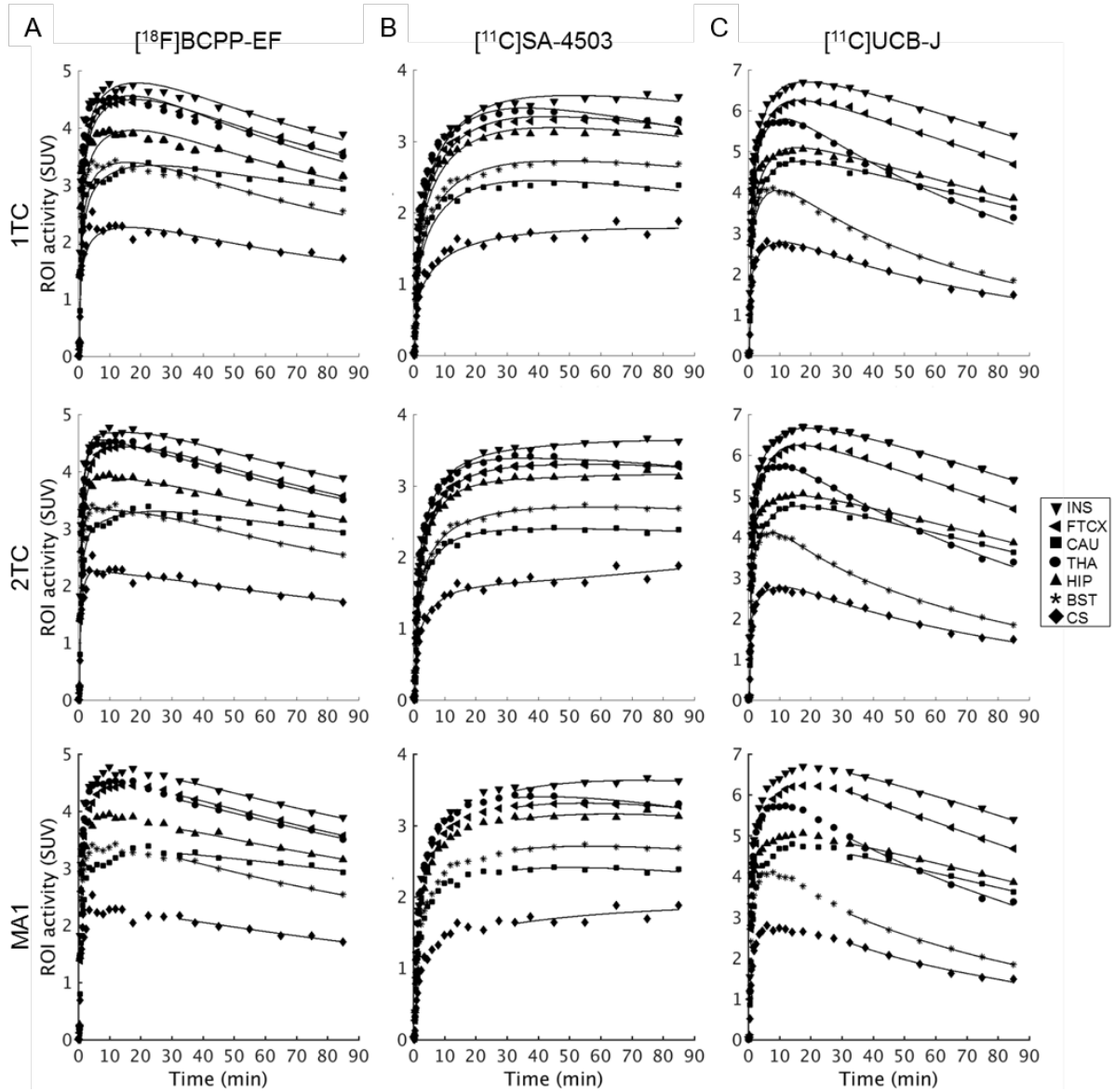

FIGURE. 3 Representative TACs and model fits for (A)[^{18}F]BCPP-EF, (B)[^{11}C]SA-4503 and (C)[^{11}C]UCB-J.

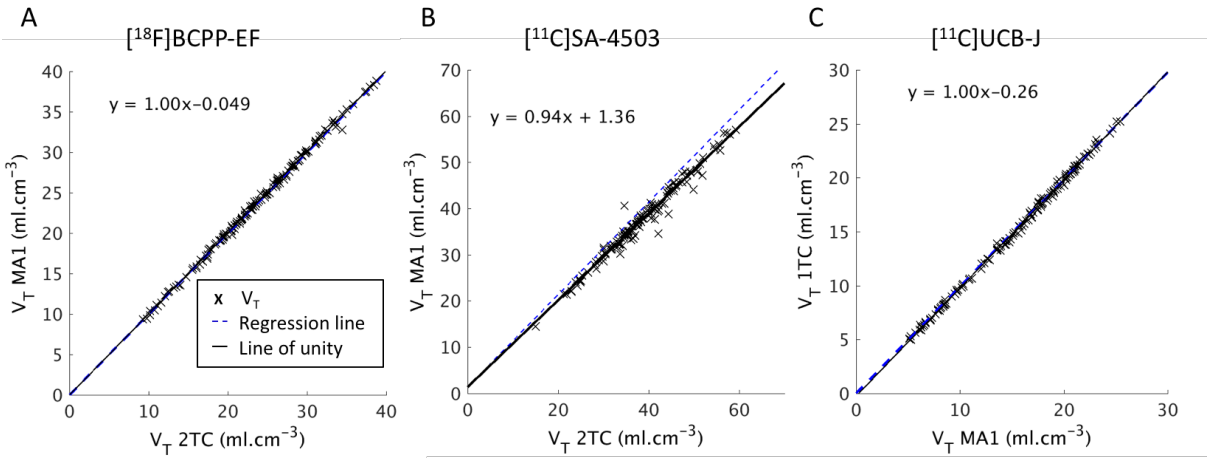

FIGURE. 4 Linear regression plots comparing (A)MA1 vs 2TC derived [^{18}F]BCPP-EF V_T, (B)MA1 vs 2TC derived [^{11}C]SA-4503 V_T, (C)MA1 vs 1TC derived [^{11}C]UCB-J V_T.

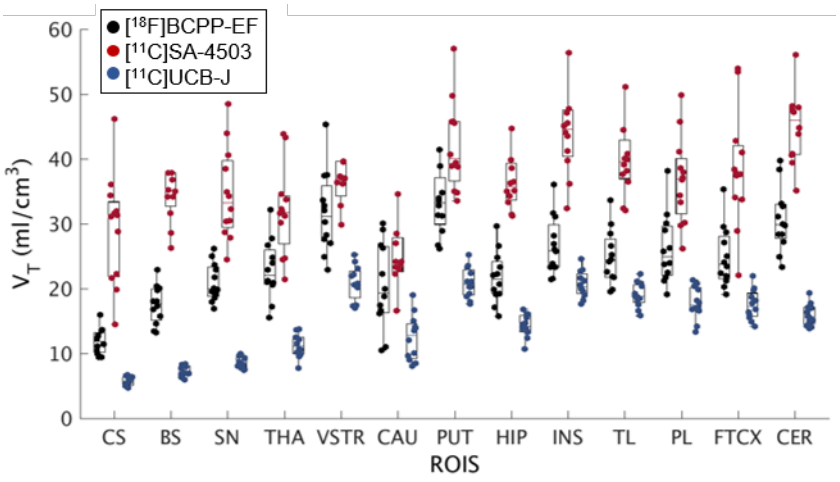

FIGURE. 5 Distribution of individual regional V_T estimates for each radioligand.

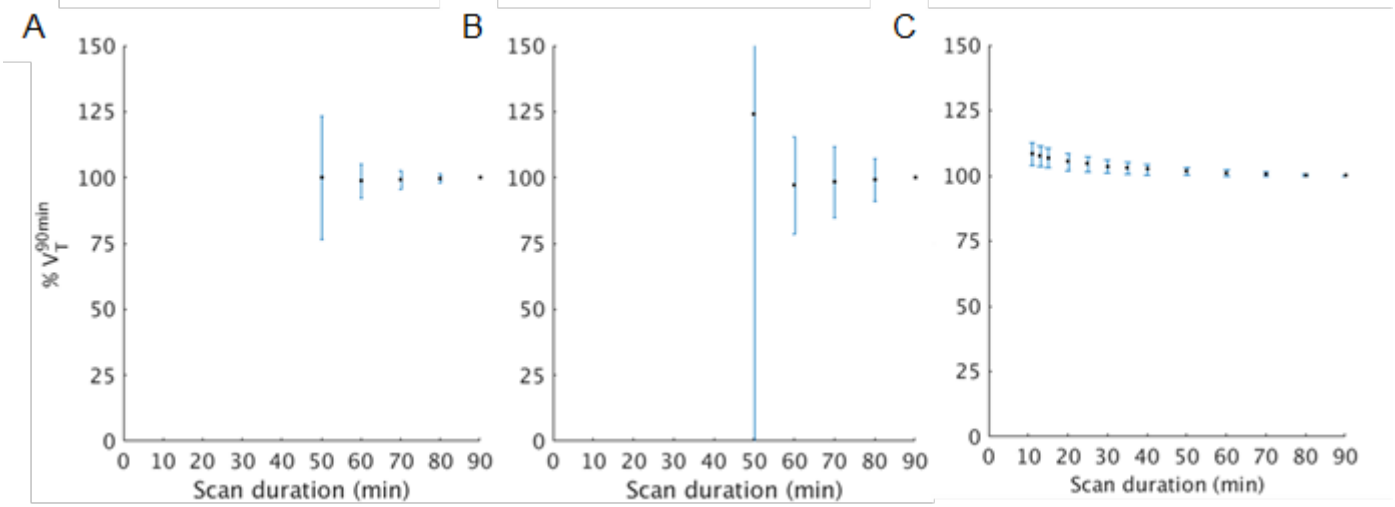

.

FIGURE. 6 Time stability plots for (A)[^{18}F]BCPP-EF V_T, (B)[^{11}C]SA-4503 V_T and (C)[^{11}C]UCB-J V_T. n = 156 data points. The first 50 minutes for [^{18}F]BCPP-EF and [^{11}C]SA-4503 have been excluded from the plots for clarity.

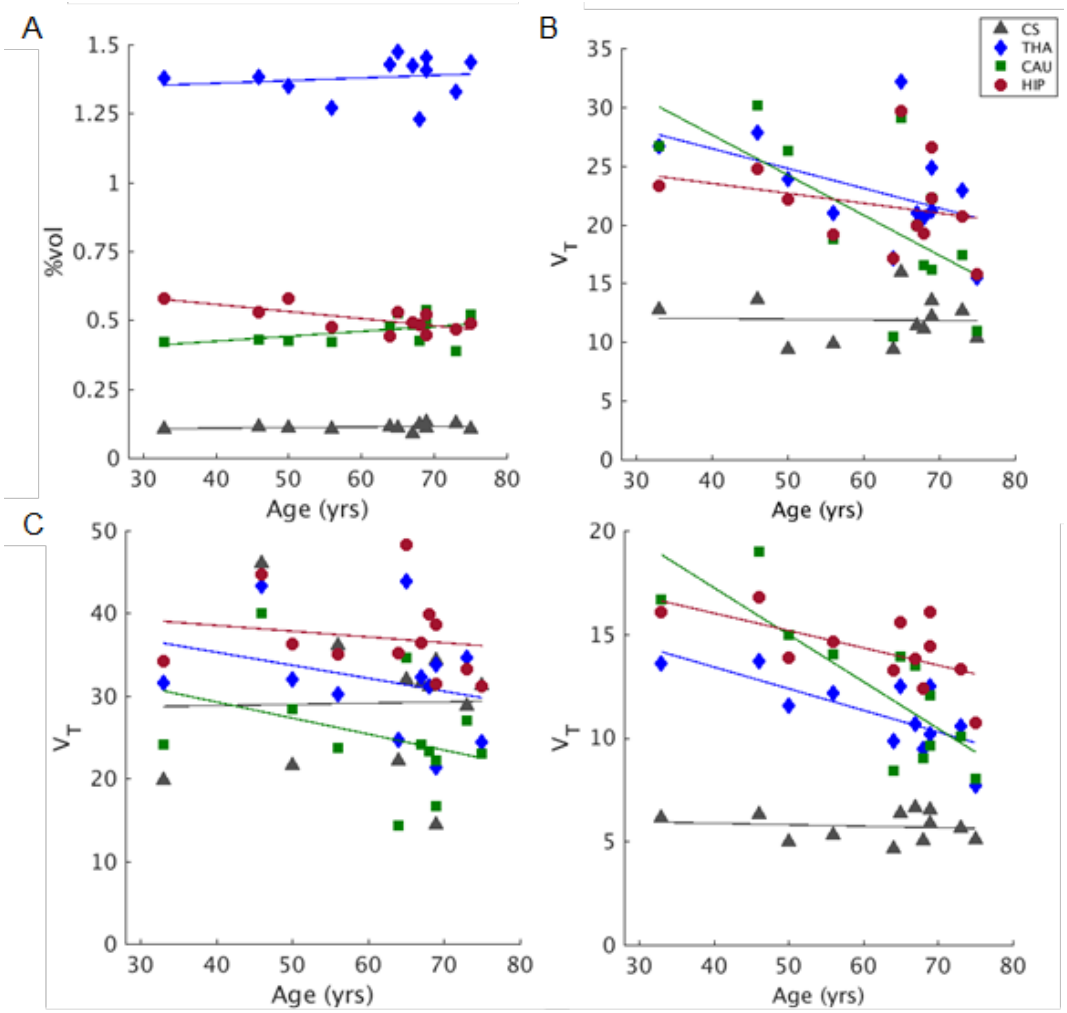

FIGURE. 7 Linear regression plots of age vs (A)%Vol_{roi}, (B)[^{18}F]BCPP-EF V_T, (C)[^{11}C]SA-4503 V_T and, (D)[^{11}C]UCB-J V_T.

TABLE 1
V_T and $\%V_{roi}$ estimates

	Radioligand	Kinetic model	ROIs												
			CS	BST	SN	THA	VST	CAU	PUT	HIP	INS	TL	PL	FTCX	CER
PET measures	[^{18}F]BCPP-EF	1TC	10.8	16.2	19.2	21	29.6	19.2	31.9	19.6	24.9	23.1	24.5	23.3	28.5
			19%	17%	14%	21%	21%	32%	20%	19%	18%	18%	21%	19%	17%
		2TC	11.9	17.5	20.9	22.8	31.6	20.4	34.1	21.6	26.5	24.7	26	24.7	30.6
			17%	17%	14%	20%	20%	32%	18%	18%	17%	17%	20%	18%	16%
		MA1	11.9	17.5	20.9	22.9	31.6	20.4	34	21.7	26.6	24.8	26.1	24.8	30.6
			17%	17%	14%	20%	20%	32%	19%	18%	17%	17%	20%	19%	16%
	[^{11}C]SA-5403	1TC	23.2	31.7	30.5	28.6	34	22	37.4	32.5	39.4	35.7	33	34.6	41.7
			23%	18%	17%	21%	21%	31%	18%	16%	15%	16%	18%	23%	17%
		2TC	26.5	37.9	34	32.7	36.8	29.4	43.8	37.9	45.9	41.5	37.7	39.4	47.7
			31%	22%	17%	22%	19%	26%	17%	15%	16%	16%	19%	23%	19%
		MA1	29.1	36.5	34.6	31.9	37.9	25.1	42.1	37	44.6	40.4	36.7	38.4	46.5
			29%	20%	21%	21%	21%	28%	16%	14%	16%	16%	18%	23%	18%
	[^{11}C]UCB-J	1TC	5.7	7.2	8.5	11.2	20.9	12.4	20.9	13.4	20.5	17.6	15.5	14	15.9
			12%	12%	10%	16%	13%	28%	11%	13%	10%	10%	14%	14%	10%
		2TC	5.9	7.4	8.9	11.4	21.2	12.6	21.1	14.6	20.9	19.3	18	17.7	16.5
			11%	11%	10%	15%	12%	28%	11%	12%	9%	9%	14%	13%	9%
		MA1	5.8	7.4	8.8	11.5	21.1	12.5	21	13.8	20.8	17.8	15.6	14.1	16.5
			12%	11%	9%	15%	12%	28%	10%	13%	9%	9%	13%	13%	9%
Volumetric Measures	-	-	0.11	2.33	0.07	1.38	0.15	0.46	0.62	0.50	0.83	8.00	6.28	5.39	6.49
			10%	5%	7%	5%	6%	11%	7%	9%	9%	6%	9%	9%	7%

PET data are mean and %COV of V_T. Volumetric data are mean and %COV of $\%V_{roi}$

TABLE 2
Age effects on volumetric and PET outcome measures

	$\%Vol_{roi}$			[^{18}F]BCPP-EF			[^{11}C]SA-4503			[^{11}C]UCB-J		
ROI	*r*	p	Δ/year	*r*	p	Δ/year	*r*	p	Δ/year	*r*	p	Δ/year
CS	0.26	0.42	0.2	-0.03	0.92	-0.05	0.02	0.95	0.05	-0.13	0.68	-0.13
BST	0.14	0.65	0.05	-0.16	0.63	-0.21	-0.22	0.49	-0.35	-0.44	0.15	-0.41
SN	-0.33	0.29	-0.17	0.02	0.94	0.03	-0.38	0.23	-0.62	-0.36	0.25	-0.28
THA	0.16	0.62	0.07	-0.46	0.13	-0.74	-0.29	0.36	-0.49	-0.74	0.01*	-0.93
VSTR	-0.18	0.57	-0.09	-0.25	0.44	-0.39	-0.24	0.45	-0.4	-0.62	0.03*	-0.63
CAU	0.46	0.14	0.39	-0.65	0.02*	-1.68	-0.35	0.26	-0.77	-0.82	0.001**	-1.83
PUT	-0.51	0.09	-0.27	-0.14	0.67	-0.21	-0.02	0.94	-0.03	-0.44	0.16	-0.39
HIP	-0.48	0.11	-0.33	-0.27	0.4	-0.39	-0.17	0.6	-0.19	-0.61	0.04*	-0.59
INS	-0.41	0.19	-0.28	-0.26	0.41	-0.35	-0.21	0.52	-0.26	-0.6	0.04*	-0.48
TL	-0.71	0.01*	-0.51	-0.26	0.42	-0.35	-0.2	0.54	-0.25	-0.55	0.06	-0.44
PL	-0.77	0.003**	-0.36	-0.32	0.31	-0.52	-0.17	0.61	-0.24	-0.61	0.03*	-0.69
FTCX	-0.75	0.01*	-0.53	-0.35	0.27	-0.52	-0.23	0.47	-0.43	-0.65	0.02*	-0.69
CER	-0.45	0.14	-0.25	0.02	0.96	0.02	-0.23	0.47	-0.33	-0.13	0.68	-0.11

r : correlation coefficient. * p<0.05; **p<0.005